Gamma-ray spectroscopy using angular distribution of Compton scattering

Andrew S. Wilhelm[a,*], Igor Jovanovic[a]

[a] *Department of Nuclear Engineering and Radiological Sciences, University of Michigan, Ann Arbor, MI 48105, USA*

Abstract

We present a novel method to perform gamma-ray spectroscopy suitable for extreme pileup situations, wherein traditional pulse-height spectroscopy is infeasible or impractical. One example of such application is spectral characterization of intense laser-based radiation sources that employ laser wakefield acceleration, in which a large number of photons can be produced in a well-collimated beam on a picosecond or shorter timescale. The method relies on the angularly-resolved calorimetric measurement of Compton scattering. The probability for a photon to undergo Compton scattering into a given solid angle is a function of its energy and is described by the Klein-Nishina formula. By first Compton scattering the incident beam and then measuring the total energies deposited in multiple detectors placed at various scattering angles, the incident beam energy spectrum can be reconstructed without resolving the individual events in detectors. We compare the performance of an maximum likelihood expectation maximization algorithm with that of an artificial neural network to measure the energy spectrum of a beam of monoenergetic gamma rays from ^{137}Cs decay. We demonstrate that the method can be used to reconstruct the characteristic inverse Compton scattering spectra.

Keywords: Gamma-ray spectroscopy, pileup, inverse Compton scattering, inverse problems

*Corresponding Author

Email addresses: andhelm@umich.edu (Andrew S. Wilhelm), ijov@umich.edu (Igor Jovanovic)

1. Introduction

Intense pulsed sources of energetic electrons, such as those based on laser wakefield acceleration [1], hold promise for a number of applications in science, industry, medicine, and security [2]. One of the distinguishing features of those new sources is their short pulse duration, which produces a high peak radiation flux. These sources can be further used in conjunction with bremsstrahlung converter targets or inverse Compton scattering (ICS) [3] to produce high-energy X rays. In ICS, the X rays can be quasi-monochromatic, continuously tunable, and produced in a well-collimated beam [3]. Typical ICS pulses can contain $\mathcal{O}(10^8)$ or more photons within the span of a few ps or shorter [4]. No available single- or few-segment detector can resolve individual photons for pulse-height spectroscopy under those conditions while operating efficiently, *i.e.*, requiring a single or few pulses to determine the pulse spectrum. Instead, an efficient detector would record a single, large sum-pulse corresponding to the total energy deposited from many nearly simultaneous photon interactions. As a result, directly resolving the spectrum is not possible using a traditional method, where the energy deposited in each interaction event is measured separately. To date, ICS spectra have been calculated from the measured spectra of the electron beams used in ICS [5], by analyzing the beam transmission through a series of lead filters [4] and similarly a stacked calorimeter [6], by Compton-scattering the beam and performing magnetic spectroscopy on the Compton electrons [7], and by using an on-axis array of CsI scintillators, and comparing the resulting distribution of scintillation light to simulation [8, 9]. Additionally, a method of directly measuring Compton-scattered photons at a single angle of scatter has been demonstrated [10], but this approach relies on high detector segmentation to prevent pileup and has low efficiency, since scattering is measured only at a single angle. We propose a new method that utilizes Compton scattering to reconstruct the photon energy spectral characteristics through analysis of the aggregate angular distribution of Compton-scattered photons measurable on a single shot and relating it to the known Klein-Nishina differential cross-section (KNDCS).

2. Theory

2.1. Klein-Nishina differential cross-section

The KNDCS, $\sigma(E, \theta)$, describes the probability for a photon of energy E to scatter into a differential solid angle and is dependent on the incident photon energy E and its scattering angle θ [11]:

$$\sigma(E,\theta) = Zr_0^2 \left[\frac{1}{1+\alpha(1-\cos\theta)}\right]^2 \left(\frac{1+\cos^2\theta}{2}\right)\left(1+\frac{\alpha^2(1-\cos\theta)^2}{(1+\cos^2\theta)[1+\alpha(1-\cos\theta)]}\right), \tag{1}$$

where Z is the atomic number of the scattering atom, r_0^2 is the classical electron radius, and $\alpha = E/m_0c^2$ is the photon energy normalized to electron rest mass equivalent energy. Representative shapes of the KNDCS for several incident photon energies ranging from 1 keV to 10 MeV are shown in Fig. 1.

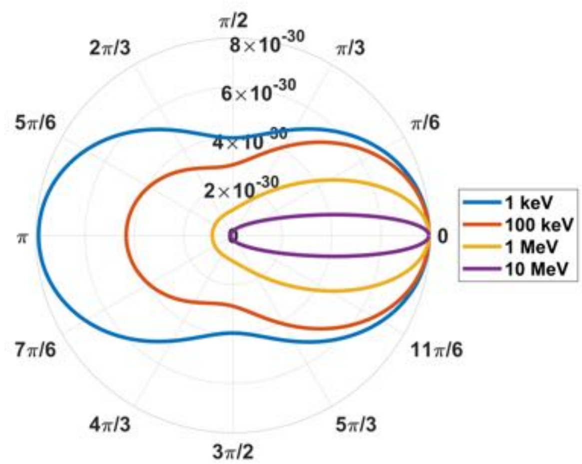

Figure 1: The Klein-Nishina differential cross-section shapes for photons of various energies scattered off a hydrogen atom. The photon is incident at $\theta = 0$ and cross-section is measured in m^2. For heavier atoms, the magnitude of the KNDCS changes, but the shape is invariant for a given photon energy. Higher energy photons are much less likely to undergo a high-angle scattering than lower energy photons.

A Compton-scattered polychromatic beam yields an angular distribution that is a superposition of the angular distributions from all spectral components that comprise the incident beam. For a continuous energy spectrum of incident photons collimated into a beam and described by $f(E) = dN/dE$, the number of photons scattered at an angle θ, $D(\theta) = dN/d\Omega$ is

$$D(\theta) = \int \sigma(E,\theta) f(E) dE, \tag{2}$$

neglecting photons that undergo multiple scattering. A photon with incident energy E scattered at angle θ has an energy

$$E'(E,\theta) = \frac{E}{(1+\alpha)(1-\cos\theta)}, \tag{3}$$

and thus the differential scattered photon energy flux $\Phi_E(\theta) = dW/d\Omega$ incident on a point detector placed at an angle θ is

$$\Phi_E(\theta) = \int \sigma(E,\theta)E'(E,\theta)f(E)dE. \tag{4}$$

The energy flux incident onto a detector placed at an angle θ is determined by an energy-integrated product of the angular distribution of scattered photons, the energy of scattered photons (which is also a function of angle and initial photon energy), and the incident beam energy spectrum $f(E)$. As a result, the shape of the angular distribution of Compton-scattered photons contains information about the energy spectrum of the incident beam.

2.2. Detector array response

The response of a detector depends not only on $\Phi_E(\theta)$, but also on its intrinsic efficiency and characteristic response function. We considered the response of a 14-detector scintillation array exposed to a scattered polychromatic photon beam. Once discretized, the array response can be modeled as

$$\begin{array}{ccccc} \mathbf{A} & & \mathbf{x} & & \mathbf{b} \\ \begin{bmatrix} a_{1,1} & \cdots & a_{1,n} \\ \vdots & \ddots & \vdots \\ a_{14,1} & \cdots & a_{14,n} \end{bmatrix} & & \begin{bmatrix} x_1 \\ \vdots \\ x_n \end{bmatrix} & = & \begin{bmatrix} b_1 \\ \vdots \\ b_{14} \end{bmatrix} \end{array} \tag{5}$$

where $\mathbf{A}$ is the detector array response matrix, in which $a_{i,j}$ is the light output in detector i per photon entering the system at energy j, x_n is the number of photons in energy bin n, and b_k is the total light output of the kth scintillation detector, which is assumed to be proportional to deposited energy. In this formulation, $\mathbf{A}$ is determined from modeling and simulation, while the light output $\mathbf{b}$ is measured experimentally. The objective is to reconstruct the binned energy distribution $\mathbf{x}$. The expected light output in detector i in terms of $\mathbf{A}$ and $\mathbf{x}$ is given by

$$b_i = a_{i,1}x_1 + a_{i,2}x_2 + ... + a_{i,n}x_n. \tag{6}$$

Note that the number of energy bins n in $\mathbf{A}$ and $\mathbf{x}$ must match but is not constrained by the number of detectors.

2.3. Solution algorithms

The response matrix, $\mathbf{A}$, has a high condition number ($\sim 10^4$ for 14 energy bins), rendering a direct and accurate solution through matrix inversion challenging [12]. Among the methods commonly applied to ill-conditioned inverse problems, least squares, regularized least squares [13], singular value decomposition [14], and Tikhonov regularization [15] were considered. While several of the methods are effective in simulating a large (>60-detector) array, they all failed with an array of more practical size such as was employed in the experimental component of this study. Another method of solving inverse problems is the maximum likelihood expectation maximization (MLEM) algorithm [16, 17]:

$$x_j^{k+1} = \frac{x_j^k}{\sum_{i=1}^{m} A_{ij}} \sum_{i=1}^{m} \frac{A_{ij} b_i}{\sum_{l=1}^{n} A_{il} x_l^k}, \tag{7}$$

where x^0 is an initial guess, here chosen as a flat positive spectrum with 100 photons/bin. This method is desirable because it does not require *a priori* knowledge of the solution, making it capable of solving general problems. The MLEM algorithm achieved the most accurate spectral reconstruction of the linear solvers we compared, but it was sensitive to noise in the measurement vector b. Another tool that can be used to solve problems of this type is an artificial neural network (ANN). While the ANN functions as a "black box", its ability to recognize patterns in the pairings of x and b vectors still relies on the same physics described in Section 2. Furthermore, the ANN demonstrated more tolerance to noise in the measured light output of the array detectors than the MLEM algorithm and was more successful in correctly reconstructing spectral shapes. The performance of an ANN is compared to that of the MLEM in Section 5.1.

3. Simulation

3.1. Response matrix

A model was developed and the response matrix was simulated in the Geant4 framework [18]. Response matrices were generated for 14, 50 ,100, 250, 500 and 1000 energy bins. Two examples of the calculated response matrices are shown in Fig. 2. The light measured in a scintillation detector was assumed to be proportional to energy deposited, since the detectors used in the experiment were previously found to exhibit a good linearity over the energy range considered [19]. Two sets of response matrices were generated. The first was made to simulate the monoenergetic experiment described in Section 4.2; 4×10^{10} photons with a flat energy spectrum in the range of 0–2000 keV were simulated. The incident photons were generated isotropically within a solid angle of 0.224 sr, such that the entire scattering target was illuminated. As described in Eq. (5), the response matrix was filled such that bin $a_{i,j}$ was the sum of all energy deposited in detector i by photons in energy bin x_j. Lastly, each bin was normalized to the number of photons within that energy range that were incident on the detector system. As expected from the shapes of the KNDCS at various energies (see Fig. 1), higher-energy photons preferentially deposit energy in detectors placed at shallower angles with respect to the incident photon direction (see Fig. 2). The second set of response matrices was generated under the same conditions described above, except the photons were emitted in a pencil beam instead of quasi-isotropically, which more accurately reflects the characteristics of an ICS beam. For the simulation to match the array response, it is necessary to include smearing and trigger thresholds. An event has a probability of triggering the detector that depends on the detector resolution and trigger threshold. For very low energy incident photons, this is impossible, which explains the empty bins in the low energy region of the 500-bin response matrix shown in Fig.2.

4. Experiment

4.1. Array design

An organic liquid scintillator (2”×2” cylindrical Eljen EJ-309) was chosen as the scattering target to strike a balance between scattering efficiency and minimizing the fraction of events that involve double scatters and photoelectric absorption [20]. The detector array comprises 14 positions for a

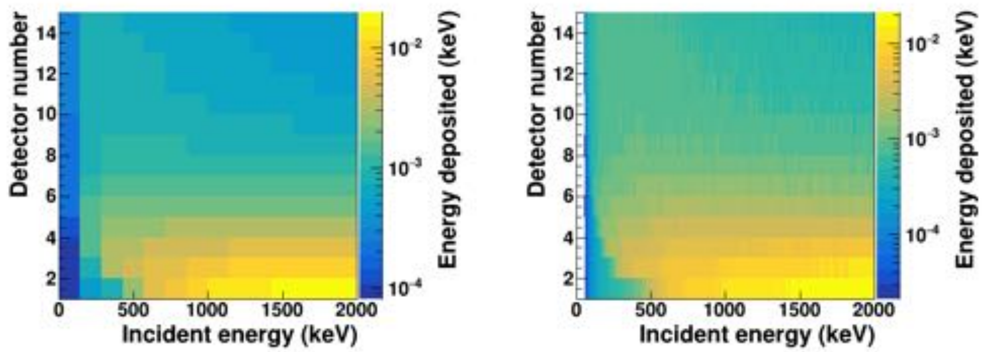

Figure 2: Simulated response matrices of (left) 14 and (right) 500 energy bins for a 14-detector array with 4×10^{10} incident photons in the range of 0–2000 keV. Detector 1 is located at a scatter angle of 12° with respect to the incident direction, and detector 14 is at a scatter angle of 168°, with detectors spaced at 12°.

2"×4"×16" NaI(Tl) scintillator, with lead shielding placed between them to prevent crosstalk. The detector positions were arranged at 12° spacing with an uncertainty of ±2°, from 12° to 168° (see Fig. 3). The distance between the source and the target was 0.75±0.05 m, and the distance between the target and array detector face was 1 ±0.05 m. The fundamental tradeoff arising in an experimental design that employs a fixed number of independent detectors (pixels) is that between efficiency and fineness of angular sampling. A statistically significant number of photons must be detected at each detector position. Thus, the expected intensity of the incident signal informs the constraints of the experimental geometry [10]. At the cost of increasing complexity, additional array detector positions could be used. A three-dimensional array could be constructed, sampling much of the sphere surrounding the target. Increasing the number of detectors will likely improve the accuracy of spectral reconstruction by reducing the impact of noise in the signal of each individual detector, but this requires an additional systematical study.

4.2. Experimental setup

For a single-shot measurement using this technique, careful calibration of the response of each array detector would be necessary. For this proof-of-concept experiment, we used a single detector and took a separate measurement at each position. The primary difference between measuring a single detector position at a time and using the entire array simultaneously

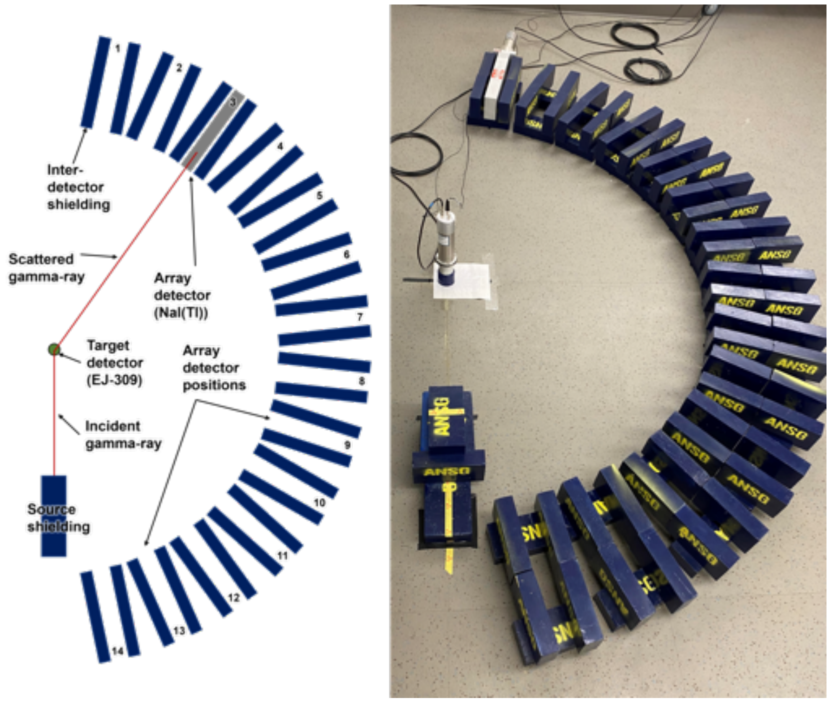

Figure 3: (left) A schematic of the experimental setup with an EJ-309 scattering target and 14 detector positions for a NaI(Tl) array detector. A photon is scattered from the target detector to detector 3. The source is inside a lead housing to shield the array detectors from direct exposure, and the detectors are shielded to prevent crosstalk. A coincidence is required between the target and a single array detector for the event to be counted. The light output of the array detector was integrated across the entire measurement time to simulate pileup. (right) A photograph of the experimental setup, with the array detector in position 1.

is the chance for a photon to scatter from one array detector to another, or crosstalk. Each detector position had two inches of lead shielding it from its neighbors to minimize crosstalk. In a full-array simulation of 10^8 661.7-keV photons, no photons deposited energy in multiple array detectors; therefore, the effect of crosstalk is negligible for the energy range used in this experiment. The trigger threshold was set to 12 keV for the target detector and 18 keV for the array detector. These thresholds were chosen to minimize low-energy events from background while still counting the lowest-energy true events. A 661.7 keV photon scattered from the target detector into the array detector at the shallowest angle (12°) deposits only 18.2 keV of energy into the target detector, however a lower threshold was required to account for the low energy resolution of EJ-309. Similarly, a 661.7 keV photon scattered into the array detector at the largest angle of scatter (168°) deposits up to 185.8° of energy. The measurements were taken with the target detector operating in coincidence mode with the array detector, with a 96-ns coincidence window. Data acquisition was performed using a CAEN V1725 digitizer with DPP-PSD firmware and the CAEN CoMPASS software. Six-hour measurements were taken using a ^{137}Cs source with an activity of 62 ± 5 µCi. The source was collimated to minimize direct irradiation of the array detector (see Fig. 3). During a 6-hour measurement, approximately 5×10^7 gamma rays were incident on the scattering detector. This integrated fluence was chosen to be representative of an ICS shot, wherein estimates for photon yield in practical experiments range from 10^7 to 10^8 [21, 22].

4.3. Data

The total energy deposited in each detector was calculated by adding the contributions from each pulse and subtracting background (including chance coincidence). The background was estimated by averaging the number of counts in each energy bin within the background region shown in Fig. 4, then multiplying that number by the width, in ns, of the integration region for that energy bin. The integration region boundaries were established by visual inspection, except for the high-energy limit, which is set to be 20% above the expected photopeak for each angle of scatter. The integrated light output for each detector position is plotted along with the results of simulation in Fig. 5. The uncertainty of the angle of scatter is 2°. The uncertainty for simulated integrated light output was determined as the standard deviation of five repeated full-array simulations of 5×10^7 661.7-keV photons. The uncertainty for experimental integrated light output, b_i in detector i, is assumed to be determined by statistics, *i.e.*, proportional to the uncertainty in the number of counts N:

$$\delta b_i = b_i/\sqrt{N} \tag{8}$$

5. Results

5.1. Monoenergetic experimental spectrum

In order to quantify the quality of reconstruction, we use cosine similarity between the discretized true and reconstructed energy spectra. The cosine

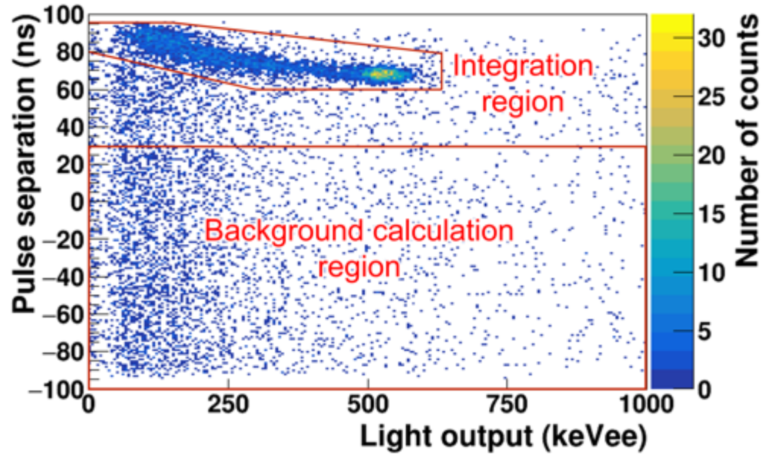

Figure 4: The light output spectrum for the array detector at a scatter angle of 36° as a function of the delay between the trigger in the scattering detector and target detector. The photopeak of scattered photons can be seen as the area of high density within the integration region at 530 keV. The delay does not represent time-of-flight of the scattered photon between the detectors, but instead a constant time offset between the channels. The regions used to calculate background and integrated light output of the array detector are marked in red.

similarity of two vectors $\mathbf{A}$ and $\mathbf{B}$ is given by

$$\text{cosine similarity} = \frac{\mathbf{A} \cdot \mathbf{B}}{\|\mathbf{A}\|\|\mathbf{B}\|}, \tag{9}$$

where a score of 0 indicates perfect orthogonality, and 1 parallel vectors. Cosine similarity is a stringent metric of comparison for high-dimensionality vectors, as it can assume a value of 0 for solutions that are off by a single energy bin. To add context, the weighted average energy of each reconstruction vector is also provided. Weighted average energy is calculated as

$$\bar{E} = \frac{\sum_{i=1}^{n} E_i x_i}{\sum_{i=1}^{n} x_i}, \tag{10}$$

where n is the number of energy bins, x_i is the number of counts in the i^{th} energy bin, and E_i is the center of the bin in keV.

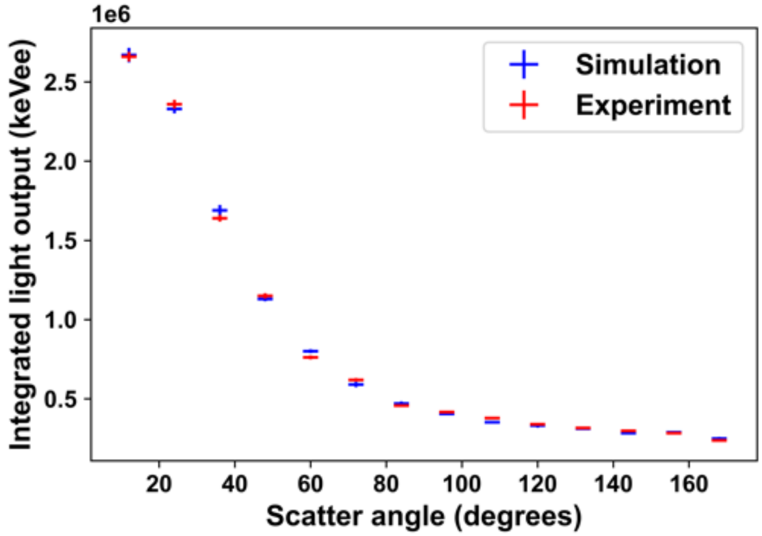

Figure 5: The experimental and simulated integrated light output for a 14-detector array exposed to a scattered beam of monoenergetic 661.7-keV photons from a 62-µCi ^{137}Cs source for 6 hours.

5.1.1. MLEM Reconstruction

The MLEM algorithm does not prioritize any particular spectral shape but rather seeks to minimize the error between experimental light output and the response matrix prediction. As such, the MLEM algorithm sometimes finds solutions with a large number of low-energy photons, such that the reconstruction is unrealistic. In order to prevent the MLEM algorithm from finding these solutions, we constrained the bottom 5% of energy bins to the value of 100.

The results of the MLEM reconstruction are shown in Fig. 6 and summarized in Table 1. In general, the MLEM algorithm fails to reconstruct a monoenergetic spectrum, with more finely-binned response matrices resulting in noiser reconstruction. However, all reconstructions with under 500 energy bins produced a weighted average energy within 3% of the true value after 2.5×10^5 iterations, and for 500 and 1000 energy bins, within 9%. Thus, this analysis technique is suitable for determining the energy centroid of a monoenergetic or quasi-monoenergetic spectrum.

Table 1: The performance of MLEM and ANN reconstruction of the spectrum of a monoenergetic ^{137}Cs source.

Energy bins	Cosine similarity		Weighted average (keV)	
	MLEM	ANN	MLEM	ANN
14	0.8008	1.0000	667.3	642.0
50	0.0000	1.0000	667.0	659.0
100	0.0000	1.0000	673.6	668.6
250	0.0000	0.8728	676.7	658.2
500	0.0000	0.0519	720.2	672.2
1000	0.0000	0.0000	711.4	644.4

5.1.2. ANN Reconstruction

Simulating a sufficient quantity of training data in Geant4 to train a neural network is computationally prohibitive. Instead, we created synthetic light output data for the detector array from random monoenergetic spectra, as described in Eq. (5), by multiplying the response matrix and spectra. To make the data realistic and to avoid repetition in the training data set, we then added Gaussian noise to the measurement vector b, with a signal-to-noise ratio (SNR) of 40. We calculate SNR as

$$SNR = b_i/\sigma_n, \tag{11}$$

where b_i is the expected value of the light output for array detector i, and σ_n is the standard deviation of the noise. The network was built using the Keras library [23] according to the specifications listed in Table 2. The results of the ANN reconstruction of the ^{137}Cs spectrum are summarized in Table 1 and shown in Fig. 7. The network was successful in reconstructing the spectrum with coarse energy bins, but the performance degraded as the number of bins increased. It should be noted that the larger response matrices had lower numbers of counts in each energy bin, and were therefore noisier (see Fig. 2). It is possible that if additional computation time is spent to generate smooth, finely binned response matrices, reconstruction with larger numbers of energy bins can be achieved.

5.2. ICS spectral reconstruction from synthetic data

The spectral shape of ICS X rays is a function of, among other parameters, electron beam energy, electron beam divergence, and laser bandwidth.

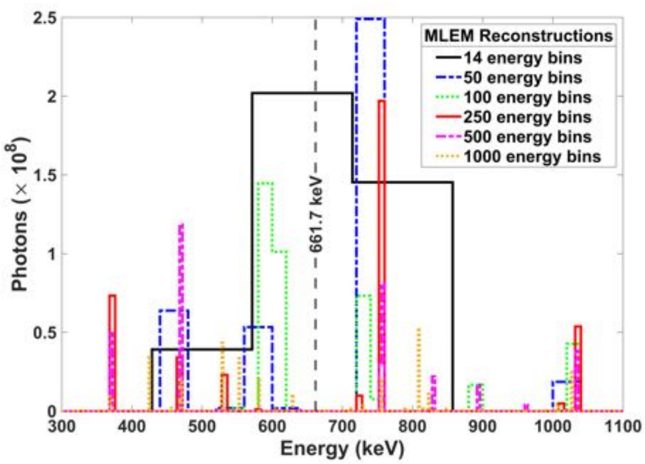

Figure 6: The results of spectral reconstruction using MLEM after 2.5×10^5 iterations with a variety of sizes of response matrices. The true incident spectrum consists of monoenergetic 661.7-keV gamma rays from ^{137}Cs. While the reconstruction of spectral shape is poor, the average energy was within 3% of the true value for 14-250 energy bins, and 9% for 500 and 1000 energy bins.

The electron beam energy primarily affects the energy centroid, while both the electron energy spread and laser bandwidth affect the width of the X-ray energy distribution. For training the neural network we simulated the ICS data by a random distribution of two parameters: a monoenergetic electron beam in the range of 175–275 MeV and a transform-limited 0.1–10 ps laser pulse. We then calculated the corresonding ICS spectrum according to the method described in Ref. [24]. The spectra are quasi-mononergetic and characteristically asymmetrical, with a low-energy tail. Unlike the monoenergetic spectra used to train the network in Section 5.1.2, the training data varied not just by centroid, but also by their width. The training data were constructed in a manner similar to the training data for the monoenergetic reconstruction. The randomized spectra were multiplied by response matrices of various sizes to obtain the light output for each detector in the array. The settings used to train the network are shown in Table 3. The test data - which the network did not see during training - were constructed through direct simulation. This was computationally feasible because the testing dataset can be much smaller than the training dataset since it is only used to evaluate the quality of the neural network. First, a random ICS spectrum was generated as described above and then used to create a prob-

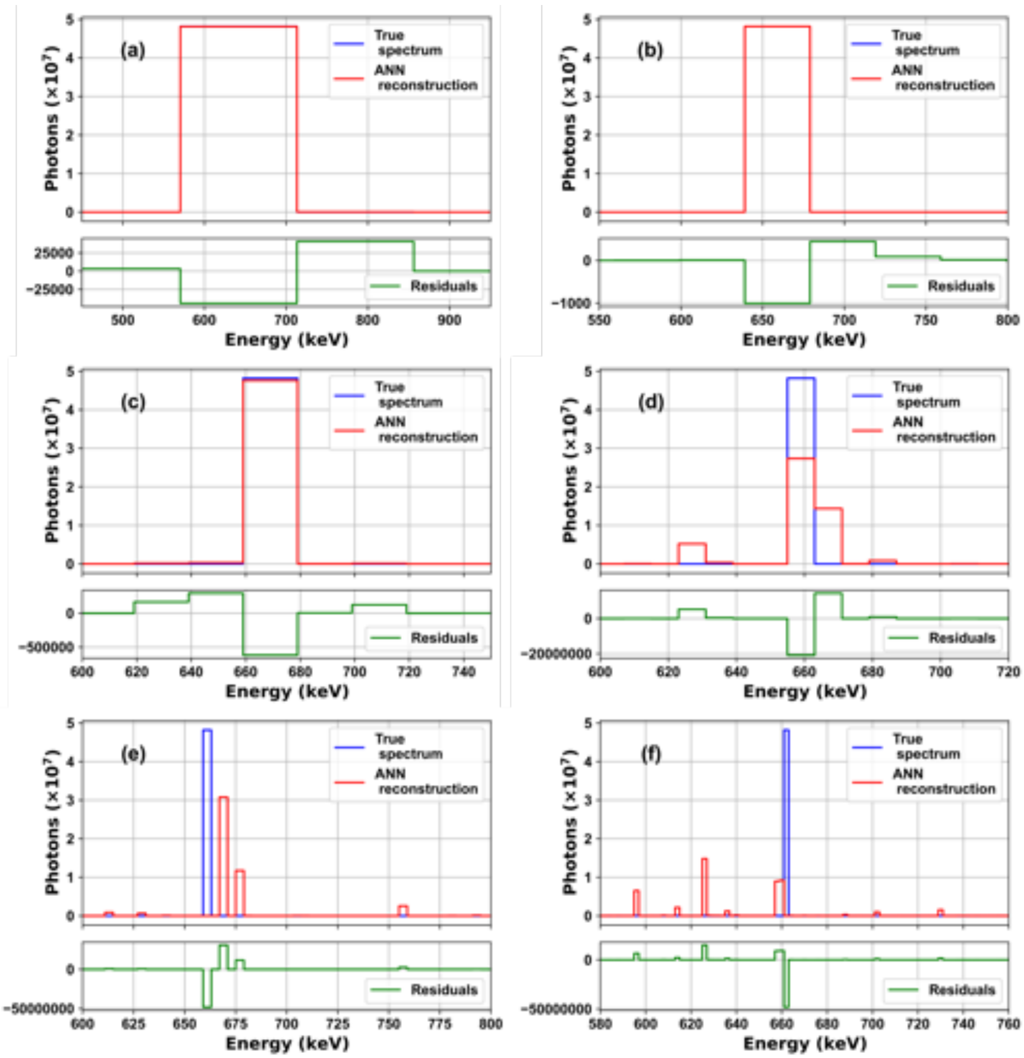

Figure 7: The results of spectral reconstruction using ANNs trained with data constructed using responses matrices of (a) 14, (b) 50, (c) 100, (d) 250, (e) 500, and (f) 1000 energy bins. The true incident spectrum was monoenergetic 661.7 keV photons from ^{137}Cs. The cosine similarities and energy weighted averages are tabulated in Table 1.

Table 2: The ANN settings used to reconstruct the monoenergetic experimental spectrum.

Setting	Value	Note
Size of training dataset	$5 \times 10^{6*}$	Constructed with an SNR of 40
Epochs	20	
Batch size	64	
Hidden layer 1	28 nodes	Sigmoid activation
Hidden layer 2	40 nodes	Sigmoid activation
Output layer	1 node/energy bin	Sigmoid activation
Loss function	Mean squared error	
Optimizer	Adam	Learning rate: 0.001

* training dataset size was 10^7 for 1000 energy bins.

ability density function. Primary particles in the simulation were created with energy sampled from this distribution. The number of photons simulated was varied and smearing was applied to the detector response to create light output spectra with different amounts of noise.

Table 3: The ANN settings used to reconstruct the ICS pulse spectra.

Setting	Value	Note
Size of training dataset	10^6	No artificial noise added
Epochs	50	
Batch size	64	
Hidden layer 1	28 nodes	Sigmoid activation
Hidden layer 2	200 nodes	Sigmoid activation
Output layer	1 node/energy bin	Sigmoid activation
Loss function	Mean squared error	
Optimizer	Adam	Learning rate: 0.001

Figure 8 shows reconstruction of ICS pulses using an ANN trained with a response matrix of 1000 energy bins. For each case, five pulses were simulated, each with the number of photons indicated. Reconstruction was performed on each, and the results were averaged. The error bars are the standard deviation of the five reconstructions. In each case, the cosine similarity was above 0.9.

It is important to note that due to the highly collimated nature of an ICS beam, the 1000 energy-bin ICS response matrix was much more efficient

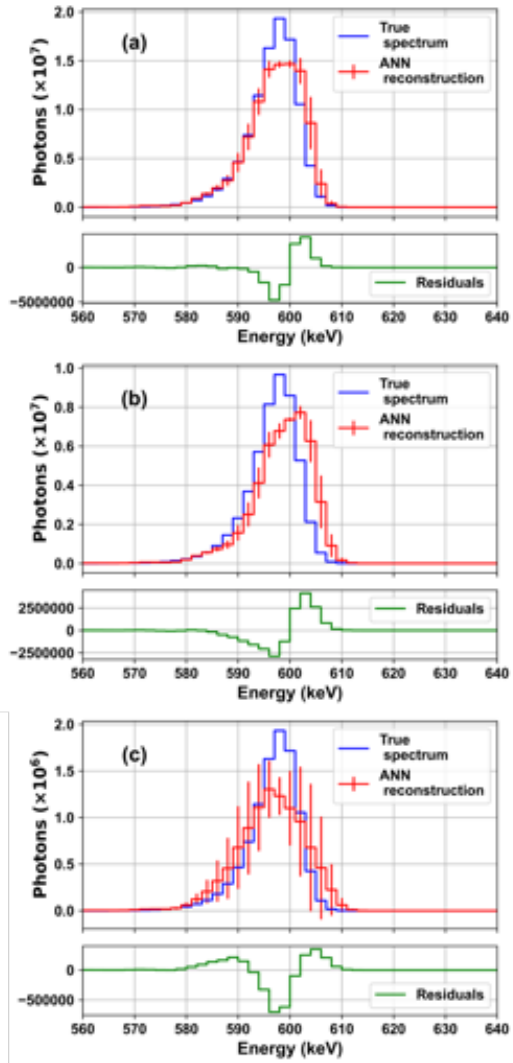

Figure 8: The results of spectral reconstruction using ANNs trained with simulated ICS pulses. A 1000 energy bin response matrix was used to train the network. ICS pulses were simulated with (a) 10^8 photons (cosine similarity: 0.9749), (b) 5×10^7 photons (cosine similarity: 0.9197) and (c) 10^7 photons (cosine similarity: 0.9537). The error bars are the standard deviation from the reconstruction of five pulses.

to simulate than for the isotropic source, and thus had more consistency between bins. This likely contributed to the better performance of the finely-binned reconstruction when compared to the experimental reconstruction of an isotropic monoenergetic ^{137}Cs source.

6. Conclusion

We demonstrated a novel technique that could be used to resolve gamma-ray spectra in a high pileup environments. The spectrum of a monochromatic beam of 662-keV gamma rays was reconstructed using two methods. The MLEM method was more consistent in reconstructing the average energy of the spectrum with coarsely-binned response matrices, but failed to reconstruct the monoenergetic shape. The ANN method was better at reconstructing the spectral shape for response matrices of 250 bins and fewer, but was still unsuccessful when more finely binned response matrices were used. The method was used along with an ANN to reconstruct simulated ICS pulses consisting of 10^7-10^8 photons with a cosine similarity above 0.9.

7. Future Work

This technique may be well-suited for short-duration, high-intensity measurements, like an ICS pulse. However, in order to use Compton array spectroscopy in this application, additional studies are required. The array must tolerate the electromagnetic pulse associated with ICS shots. The scintillator and light sensor (*e.g.*, photomultiplier) response to large sum-pulses needs to be well understood. Among the possible sources of nonlinearity are photocathode bleaching and dynode space charge effects [25]. In some situations, filters between the scintillating crystal and photocathode [26], PMTs that operate with low gain [27], or low light-producing detectors [28] may be needed to avoid saturation, all of which could be accounted for in response matrix generation.

In our work, the scattering target was chosen to be a detector so that we could use coincidence between the target and array to filter out background for our long measurements. However, in a short-pulse measurement, the target need not be a detector, but could be an inert object optimized for efficiency of Compton scattering. For instance, a hydrocarbon target would have favorable Compton scattering properties while minimizing pair production.

Additionally, experimental work with larger arrays should be performed to confirm that more precise and accurate results are achievable.

Lastly, the parameter space for the an ICS beam is large, and we have investigated only a fraction of it here. For instance, the photon energy in an ICS beam can be broader than we considered, and can have an angular dependence [29] that we did not model. This technique should be investigated for stability under these conditions.

8. Acknowledgements

This work was supported in part by Department of Energy National Nuclear Security Administration, Consortium for Monitoring, Technology, and Verification (DE-NA0003920); Department of Defense, Defense Threat Reduction Agency (HDTRA1-20-2-0002); and high-performance computer time and resources from the DoD High Performance Computing Modernization Program.

References

[1] E. Esarey, C. B. Schroeder, W. P. Leemans, Physics of laser-driven plasma-based electron accelerators, Reviews of Modern Physics 81 (2009) 1229–1285.

[2] F. Albert, A. G. Thomas, Applications of laser wakefield accelerator-based light sources, Plasma Physics and Controlled Fusion 58 (2016).

[3] F. V. Hartemann, D. J. Gibson, W. J. Brown, A. Rousse, K. T. Phuoc, V. Mallka, J. Faure, A. Pukhov, Compton scattering x-ray sources driven by laser wakefield acceleration, Physical Review Special Topics - Accelerators and Beams 10 (2007) 11301.

[4] S. Banerjee, S. Chen, N. Powers, D. Haden, C. Liu, G. Golovin, J. Zhang, B. Zhao, S. Clarke, S. Pozzi, J. Silano, H. Karwowski, D. Umstadter, Compact source of narrowband and tunable X-rays for radiography, Nuclear Instruments and Methods in Physics Research, Section B: Beam Interactions with Materials and Atoms 350 (2015) 106–111.

[5] S. Chen, G. Golovin, C. Miller, D. Haden, S. Banerjee, P. Zhang, C. Liu, J. Zhang, B. Zhao, S. Clarke, S. Pozzi, D. Umstadter, Shielded radiography with a laser-driven MeV-energy X-ray source, Nuclear Instruments

and Methods in Physics Research, Section B: Beam Interactions with Materials and Atoms 366 (2016) 217–223.

[6] A. Hannasch, A. Laso Garcia, M. LaBerge, R. Zgadzaj, A. Köhler, J. P. Couperus Cabadağ, O. Zarini, T. Kurz, A. Ferrari, M. Molodtsova, L. Naumann, T. E. Cowan, U. Schramm, A. Irman, M. C. Downer, Compact spectroscopy of keV to MeV X-rays from a laser wakefield accelerator, Scientific Reports 11 (2021) 1–17.

[7] D. J. Corvan, G. Sarri, M. Zepf, Design of a compact spectrometer for high-flux MeV gamma-ray beams, Review of Scientific Instruments 85 (2014) 65119.

[8] J. M. Cole, K. T. Behm, E. Gerstmayr, T. G. Blackburn, J. C. Wood, C. D. Baird, M. J. Duff, C. Harvey, A. Ilderton, A. S. Joglekar, K. Krushelnick, S. Kuschel, M. Marklund, P. McKenna, C. D. Murphy, K. Poder, C. P. Ridgers, G. M. Samarin, G. Sarri, D. R. Symes, A. G. Thomas, J. Warwick, M. Zepf, Z. Najmudin, S. P. Mangles, Experimental Evidence of Radiation Reaction in the Collision of a High-Intensity Laser Pulse with a Laser-Wakefield Accelerated Electron Beam, Physical Review X 8 (2018) 011020.

[9] K. T. Behm, J. M. Cole, A. S. Joglekar, E. Gerstmayr, J. C. Wood, C. D. Baird, T. G. Blackburn, M. Duff, C. Harvey, A. Ilderton, S. Kuschel, S. P. Mangles, M. Marklund, P. McKenna, C. D. Murphy, Z. Najmudin, K. Poder, C. P. Ridgers, G. Sarri, G. M. Samarin, D. Symes, J. Warwick, M. Zepf, K. Krushelnick, A. G. Thomas, A spectrometer for ultrashort gamma-ray pulses with photon energies greater than 10 MeV, Review of Scientific Instruments 89 (2018).

[10] S. Cipiccia, S. M. Wiggins, D. Maneuski, E. Brunetti, G. Vieux, X. Yang, R. C. Issac, G. H. Welsh, M. Anania, M. R. Islam, B. Ersfeld, R. Montgomery, G. Smith, M. Hoek, D. J. Hamilton, N. R. Lemos, D. R. Symes, P. P. Rajeev, V. O. Shea, J. M. Dias, D. A. Jaroszynski, Compton scattering for spectroscopic detection of ultra-fast, high flux, broad energy range X-rays, Review of Scientific Instruments 84 (2013) 113302.

[11] O. Klein, T. Nishina, Über die Streuung von Strahlung durch freie Elektronen nach der neuen relativistischen Quantendynamik von Dirac, Zeitschrift für Physik 52 (1929) 853–868.

[12] P. C. Hansen, The discrete picard condition for discrete ill-posed problems, Bit 30 (1990) 658–672.

[13] P. C. Hansen, Regularization Tools version 4.0 for Matlab 7.3, Numerical Algorithms 46 (2007) 189–194.

[14] P. C. Hansen, Truncated Singular Value Decomposition Solutions to Discrete Ill-Posed Problems with Ill-Determined Numerical Rank, SIAM Journal on Scientific and Statistical Computing 11 (1990) 503–518.

[15] G. H. Golub, P. C. Hansen, D. P. O'Leary, Tikhonov regularization and total least squares, SIAM Journal on Matrix Analysis and Applications 21 (1999) 185–194.

[16] A. P. Dempster, N. M. Laird, D. B. Rubin, Maximum Likelihood from Incomplete Data Via the EM Algorithm , Journal of the Royal Statistical Society: Series B (Methodological) 39 (1977) 1–22.

[17] H. Q. Zhu, H. Z. Shu, J. Zhou, L. M. Luo, Maximum likelihood algorithm for PET image reconstruction based on fuzzy random variable, in: Annual International Conference of the IEEE Engineering in Medicine and Biology - Proceedings, volume 26 II, pp. 1361–1364.

[18] S. Agostinelli, J. Allison, K. Amako, J. Apostolakis, H. Araujo, P. Arce, M. Asai, D. Axen, S. Banerjee, G. Barrand, F. Behner, L. Bellagamba, J. Boudreau, L. Broglia, A. Brunengo, H. Burkhardt, S. Chauvie, J. Chuma, R. Chytracek, G. Cooperman, G. Cosmo, P. Degtyarenko, A. Dell'Acqua, G. Depaola, D. Dietrich, R. Enami, A. Feliciello, C. Ferguson, H. Fesefeldt, G. Folger, F. Foppiano, A. Forti, S. Garelli, S. Giani, R. Giannitrapani, D. Gibin, J. J. Gomez Cadenas, I. Gonzalez, G. Gracia Abril, G. Greeniaus, W. Greiner, V. Grichine, A. Grossheim, S. Guatelli, P. Gumplinger, R. Hamatsu, K. Hashimoto, H. Hasui, A. Heikkinen, A. Howard, V. Ivanchenko, A. Johnson, F. W. Jones, J. Kallenbach, N. Kanaya, M. Kawabata, Y. Kawabata, M. Kawaguti, S. Kelner, P. Kent, A. Kimura, T. Kodama, R. Kokoulin, M. Kossov, H. Kurashige, E. Lamanna, T. Lampen, V. Lara, V. Lefebure, F. Lei, M. Liendl, W. Lockman, F. Longo, S. Magni, M. Maire, E. Medernach, K. Minamimoto, P. Mora de Freitas, Y. Morita, K. Murakami, M. Nagamatu, R. Nartallo, P. Nieminen, T. Nishimura, K. Ohtsubo, M. Okamura, S. O'Neale, Y. Oohata, K. Paech, J. Perl, A. Pfeiffer,

M. G. Pia, F. Ranjard, A. Rybin, S. Sadilov, E. di Salvo, G. Santin, T. Sasaki, N. Savvas, Y. Sawada, S. Scherer, S. Sei, V. Sirotenko, D. Smith, N. Starkov, H. Stoecker, J. Sulkimo, M. Takahata, S. Tanaka, E. Tcherniaev, E. Safai Tehrani, M. Tropeano, P. Truscott, H. Uno, L. Urban, P. Urban, M. Verderi, A. Walkden, W. Wander, H. Weber, J. P. Wellisch, T. Wenaus, D. C. Williams, D. Wright, T. Yamada, H. Yoshida, D. Zschiesche, GEANT4 - A simulation toolkit, Nuclear Instruments and Methods in Physics Research, Section A: Accelerators, Spectrometers, Detectors and Associated Equipment 506 (2003) 250–303.

[19] P. L. Reeder, D. C. Stromswold, Performance of Large NaI(Tl) Gamma-Ray Detectors Over Temperature -50ºC to +60ºC, Pacific Northwest National Laboratory 14735 (2004) 1–46.

[20] F. Pino, L. Stevanato, D. Cester, G. Nebbia, L. Sajo-Bohus, G. Viesti, The light output and the detection efficiency of the liquid scintillator EJ-309, Applied Radiation and Isotopes 89 (2014) 79–84.

[21] R. Kuroda, H. Toyokawa, M. Yasumoto, H. Ikeura-Sekiguchi, M. Koike, K. Yamada, T. Yanagida, T. Nakajyo, F. Sakai, K. Mori, Quasi-monochromatic hard X-ray source via laser Compton scattering and its application, Nuclear Instruments and Methods in Physics Research, Section A: Accelerators, Spectrometers, Detectors and Associated Equipment 637 (2011) S183–S186.

[22] K. Ta Phuoc, S. Corde, C. Thaury, V. Malka, A. Tafzi, J. P. Goddet, R. C. Shah, S. Sebban, A. Rousse, All-optical Compton gamma-ray source, Nature Photonics 6 (2012) 308–311.

[23] F. Chollet, others, Keras, 2015.

[24] F. V. Hartemann, W. J. Brown, D. J. Gibson, S. G. Anderson, A. M. Tremaine, P. T. Springer, A. J. Wootton, E. P. Hartouni, C. P. Barty, High-energy scaling of Compton scattering light sources, Physical Review Special Topics - Accelerators and Beams 8 (2005) 1–28.

[25] C. Knappe, J. Lindén, F. Abou Nada, M. Richter, M. Aldén, Investigation and compensation of the nonlinear response in photomultiplier

tubes for quantitative single-shot measurements, Review of Scientific Instruments 83 (2012) 34901.

[26] P. R. Menge, G. Gautier, A. Iltis, C. Rozsa, V. Solovyev, Performance of large lanthanum bromide scintillators, Nuclear Instruments and Methods in Physics Research, Section A: Accelerators, Spectrometers, Detectors and Associated Equipment 579 (2007) 6–10.

[27] F. G. Quarati, A. Owens, P. Dorenbos, J. T. De Haas, G. Benzoni, N. Blasi, C. Boiano, S. Brambilla, F. Camera, R. Alba, G. Bellia, C. Maiolino, D. Santonocito, M. Ahmed, N. Brown, S. Stave, H. R. Weller, Y. K. Wu, High energy gamma-ray spectroscopy with LaBr3 scintillation detectors, Nuclear Instruments and Methods in Physics Research, Section A: Accelerators, Spectrometers, Detectors and Associated Equipment 629 (2011) 157–169.

[28] D. B. Cassidy, A. P. Mills, A fast detector for single-shot positron annihilation lifetime spectroscopy, Nuclear Instruments and Methods in Physics Research, Section A: Accelerators, Spectrometers, Detectors and Associated Equipment 580 (2007) 1338–1343.

[29] F. Albert, S. G. Anderson, D. J. Gibson, C. A. Hagmann, M. S. Johnson, M. Messerly, V. Semenov, M. Y. Shverdin, B. Rusnak, A. M. Tremaine, F. V. Hartemann, C. W. Siders, D. P. McNabb, C. P. Barty, Characterization and applications of a tunable, laser-based, MeV-class Compton-scattering γ-ray source, Physical Review Special Topics - Accelerators and Beams 13 (2010) 1–13.